Monitoring increases in fracture connectivity during hydraulic stimulations from temporal variations in shear wave splitting polarization

Alan F. Baird,[1] J.-Michael Kendall,[1] James P. Verdon,[1] Andreas Wuestefeld,[2]
Todd E. Noble,[3] Yongyi Li,[4] Martin Dutko[5] and Quentin J. Fisher[6]

[1]*School of Earth Sciences, University of Bristol, Bristol, United Kingdom. E-mail: alan.baird@bristol.ac.uk*
[2]*NORSAR, Gunnar Randers vei* 15, 2007 *Kjeller, Norway*
[3]*Nederlandse Aardolie Maatschappij B.V., Assen, the Netherlands*
[4]*Shell Canada, Calgary, Alberta, Canada*
[5]*Rockfield Software Limited, Swansea, United Kingdom*
[6]*Centre for Integrated Petroleum Engineering and Geoscience, School of Earth and Environment, University of Leeds, Leeds, United Kingdom*

GJI Seismology

SUMMARY

Hydraulic overpressure can induce fractures and increase permeability in a range of geological settings, including volcanological, glacial and petroleum reservoirs. Here we consider an example of induced hydraulic fracture stimulation in a tight-gas sandstone. Successful exploitation of tight-gas reservoirs requires fracture networks, either naturally occurring, or generated through hydraulic stimulation. The study of seismic anisotropy provides a means to infer properties of fracture networks, such as the dominant orientation of fracture sets and fracture compliances. Shear wave splitting from microseismic data acquired during hydraulic fracture stimulation allows us to not only estimate anisotropy and fracture properties, but also to monitor their evolution through time. Here, we analyse shear wave splitting using microseismic events recorded during a multistage hydraulic fracture stimulation in a tight-gas sandstone reservoir. A substantial rotation in the dominant fast polarization direction (ψ) is observed between the events of stage 1 and those from later stages. Although large changes in ψ have often been linked to stress-induced changes in crack orientation, here we argue that it can better be explained by a smaller fracture rotation coupled with an increase in the ratio of normal to tangential compliance (Z_N/Z_T) from 0.3 to 0.6. Z_N/Z_T is sensitive to elements of the internal architecture of the fracture, as well as fracture connectivity and permeability. Thus, monitoring Z_N/Z_T with shear wave splitting can potentially allow us to remotely detect changes in permeability caused by hydraulic stimulation in a range of geological settings.

**Key words:** Downhole methods; Fracture and flow; Seismic anisotropy.

1 INTRODUCTION

The development of fracture networks is a geological process that can significantly enhance permeability of a material. Examples include magma migration in volcanological settings, water drainage in ice sheets and petroleum migration in sedimentary rocks. All are examples of hydraulic stimulation in response to stress changes. Here we show how the seismic monitoring of shear wave splitting can be used to infer the development of fracture networks with an example of hydraulic stimulation in a tight-gas sandstone.

The hydrocarbon industry is moving increasingly towards unconventional resources, such as tight sandstone and shale gas. These reservoirs have very low natural permeabilities and require fractures, either natural or induced through hydraulic stimulation, in order to be produced economically. By providing additional pathways

for fluid flow, fractures can significantly enhance the permeability of a reservoir, and therefore increase production. The ability to detect and characterize fractures *in situ* is therefore of great importance. Although seismic studies lack the resolution required to directly image individual fractures, the presence of aligned fracture sets will render the bulk rock seismically anisotropic, provided the fracture spacing and size is much smaller than that of the dominant wavelength (e.g. Hudson 1980; Crampin 1984; Hall & Kendall 2003). Detection and characterization of this anisotropy can therefore be used to infer fracture properties.

In addition to fractures, other factors may also contribute to the anisotropy of sedimentary rocks. For example, the periodic layering of sedimentary strata (e.g. Backus 1962) and the preferred alignment of intrinsically anisotropic minerals (e.g. Vernik & Nur 1992; Valcke *et al.* 2006; Kendall *et al.* 2007) may contribute to anisotropy
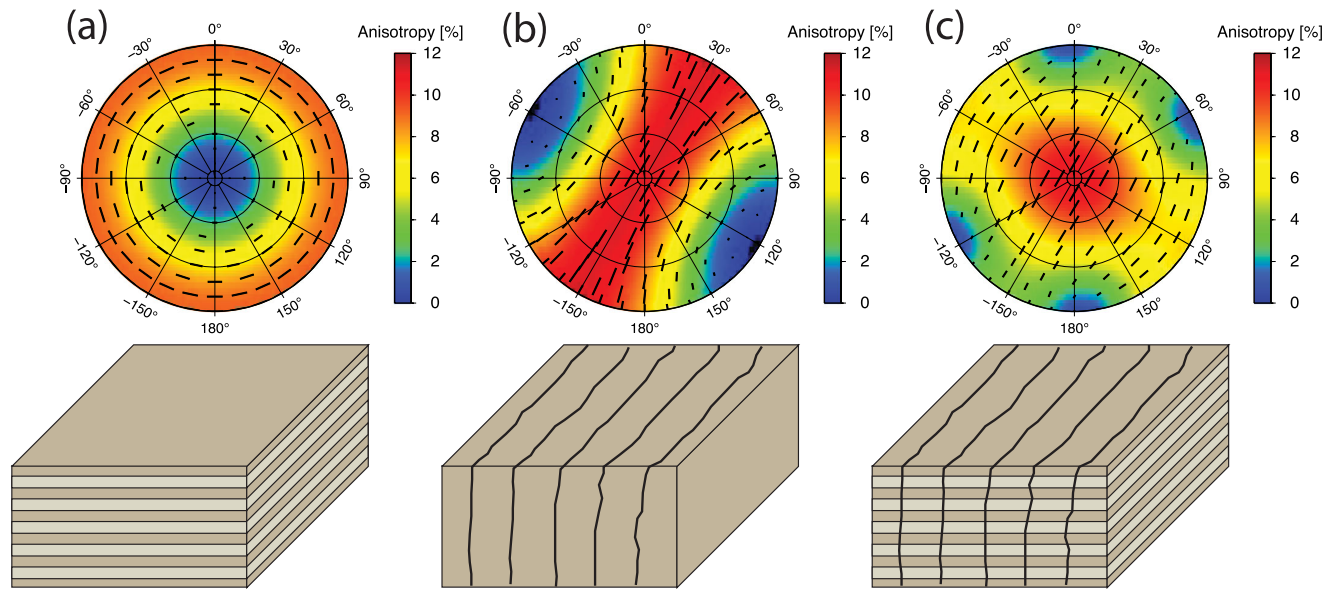
Figure 1. Synthetic upper hemisphere plots showing SWS magnitude, δV_S (contours and tick lengths), and fast wave polarization, ψ (black tick orientations) for: (a) VTI anisotropy due to horizontal layering/fabric; (b) HTI anisotropy due to aligned vertical fractures and (c) orthorhombic anisotropy due to vertical fractures in a horizontally layered medium.

related to the rock fabric. Differing sources of anisotropy may be distinguished by making some simplifying assumptions about their respective orientation and symmetry. Sedimentary fabric, for example, is often controlled by the horizontal alignment of phyllosilicate minerals, which will produce anisotropy with hexagonal symmetry with a vertical axis of symmetry (vertical transverse isotropy, VTI) (e.g. Kendall *et al.* 2007). Conversely, fracture sets are typically steeply dipping or vertical, which will produce horizontal transverse isotropy (HTI). The combined effect of both rock fabric and aligned fractures produces bulk anisotropy with orthorhombic symmetry (e.g. Verdon *et al.* 2009) (Fig. 1).

Many techniques are available for estimating seismic anisotropy. For example, through the detection of azimuthal variations in reflection amplitudes (e.g. Lynn & Thomsen 1990; Hall & Kendall 2003), or non-hyperbolic moveout velocities (e.g. Tsvankin & Thomsen 1994; Alkhalifah 1997; van der Baan & Kendall 2002). However, shear wave splitting provides perhaps the least ambiguous indicator of anisotropy. When a shear wave passes through an anisotropic medium, it will split into two orthogonally polarized waves travelling at different velocities. The polarization of the fast wave (ψ) and slow wave are indicators of the anisotropic symmetry of the medium, while the delay time between the arrivals (δt) is proportional to magnitude and extent of the anisotropy. The delay time is often normalized by the path length, to express anisotropy as a percentage difference in velocity between the fast and slow waves (δV_S). The measurement of these parameters for a range of propagation directions can be used to fully characterize the anisotropy of the medium, which can then be interpreted in terms of rock fabric and fractures.

In recent years there has been rapid growth in the use of passive seismic techniques as a means to monitor hydraulic fracture stimulations (e.g. Maxwell 2010). As fractures propagate during stimulation, they generate microseismic events that can be detected using downhole geophone arrays or large arrays of surface sensors (e.g. Chambers *et al.* 2010). The main objective of these studies is to locate the events as accurately as possible and thereby map the extent and complexity of the induced fractures. Since microseismic events produce very strong shear waves, they make excellent sources for

shear wave splitting analysis. The data can therefore be used to infer anisotropy, which can be interpreted in terms of fracture properties in the region surrounding the main hydraulic fracture stimulation. In addition, given the large number of microseismic events associated with hydraulic stimulation, it may be possible to monitor changes in anisotropy that can give an indication of the evolution of the induced fracture network (e.g. Wuestefeld *et al.* 2011; Verdon & Wüstefeld 2013).

Here we study shear wave splitting during a multistage hydraulic fracture stimulation in a tight-gas sandstone field in North America. Because of confidentiality agreements we cannot divulge the location of the field.

2 BACKGROUND

Fig. 2 shows a layout of the stimulation project, and a summary of the located events. To monitor the stimulation, a receiver array composed of 11 three-component geophones, spaced at 11.2 m intervals was installed in a nearby well, approximately 400 m to the SE of the treatment well. The geophones were placed such that the bottom instrument was above the interval of interest. The treatment well was stimulated for gas production over six stages, beginning at the base and moving upward, with 2–5 d breaks between each stage. A gelled frac oil system was used in all stages, and was pumped at rates between 4.5 and 6.0 m^3 min^{-1} using a ceramic proppant to keep the induced fractures open. In total, there were 799 located events that form a linear trend indicating the growth of a fracture network oriented northeast–southwest ($\sim$45°), subparallel to S_H, the orientation of maximum horizontal compressive stress.

Borehole image logs taken from the treatment well prior to the fracture stimulation provide some constraints on the *in situ* stresses and natural fracture properties. Fig. 3 shows the distribution of borehole breakout azimuths within the well, which provides an estimate of the orientation of S_H. The data show some indication of variation of stress with depth. Breakouts deeper than 3300 m have a mean orientation of $\sim$37 $\pm$ 5°, conversely, in shallower portions of the well there is a clockwise rotation in the mean orientation as
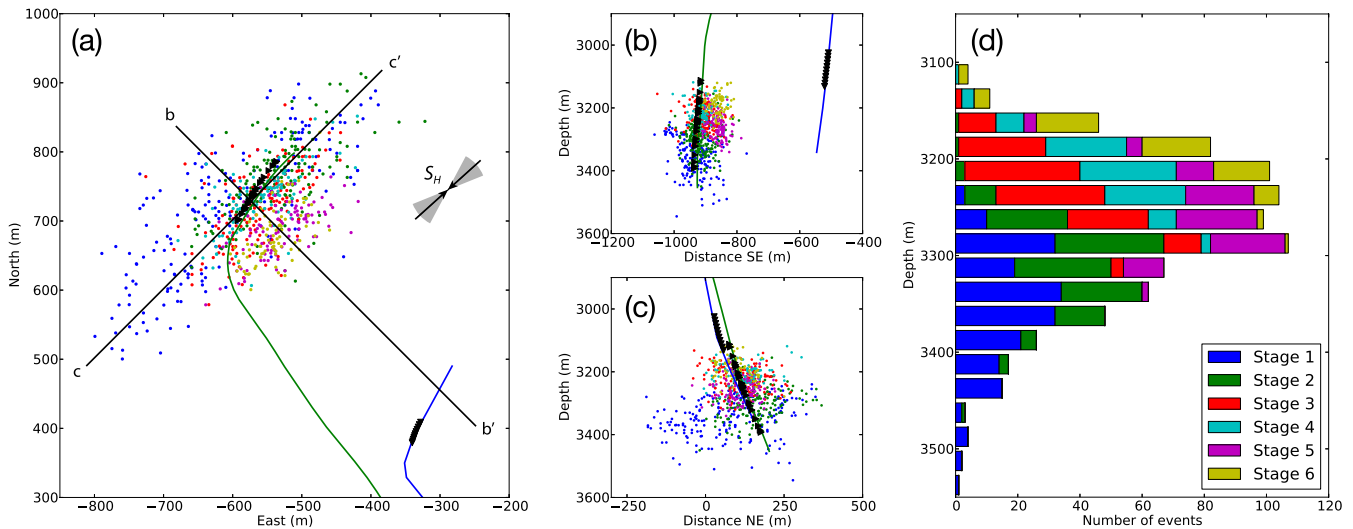
Figure 2. Event locations and geometry of treatment well (green) and receiver well (blue) in map view (a), and cross-sectional views cutting across the strike (b), and along the strike (c) of the main seismicity cloud. Events are coloured by stage number. Lines b–b′ and c–c′ in (a) indicate the locations of cross-sections in (b) and (c), respectively. The maximum horizontal compressive stress orientation is indicated by S_H. (d) Histogram showing depth distribution of the events. While each successive stage is shallower, there is significant overlap in event depths.
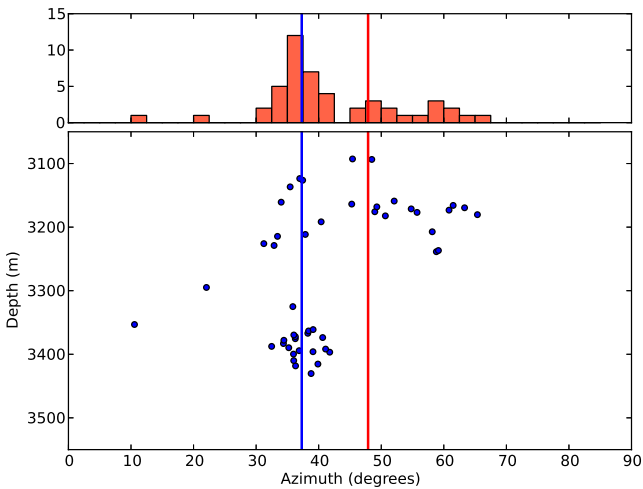
Figure 3. Borehole breakout azimuths from the treatment well prior to the fracture stimulation. The mean azimuth, which may be used as a proxy for the orientation of the maximum horizontal compressive stress (S_H), is approximately 42°. However, the breakouts do show some depth variation with a wider variance in azimuth in the shallow portions ($\sim$48 ± 15°) than in the deeper portions ($\sim$37 ± 5°). Blue and red lines indicate mean breakout orientation for the deep ($>$3300 m) and shallow ($<$3300 m) measurements, respectively.

well as a wider variance ($\sim$48 ± 15°), possibly indicating reduced stress anisotropy.

Fig. 4 shows the distribution of natural open fractures in the treatment well prior to hydraulic stimulation. Most fractures are steeply dipping and consistently strike approximately 35°, throughout the depth range of interest. Between the depths of 3250 and 3300 m there is a wider scatter in strike orientations, but these are mainly moderate to shallow dipping fractures indicating a localized damage zone. This damage zone coincides with the apparent change in stress field inferred from the breakout data (Fig. 3). Interestingly, the steep fracture orientation does not show a similar depth varia-

tion, deep fractures are subparallel to S_H, while shallow fracture are more oblique (by $\sim$10–15°) to the rotated stress field.

3 SHEAR WAVE SPLITTING

The data set was processed for shear wave splitting to provide a measure of anisotropy along the source–receiver ray path. The data were analysed using the automated splitting approach of Wuestefeld *et al.* (2010). This method allows for the easy processing of large data sets, and provides quality control in the form of a quality index which varies from -1.0 for null measurements, to 0.0 for poor and $+1.0$ for good measurements. The quality index is based on differences in splitting parameters obtained using the cross-correlation technique versus the eigenvalue method. The ideal 'good' measurement are characterized by identical splitting parameters from each method (see Wuestefeld *et al.* 2010, for further details). Over the six simulation stages, 3985 source–receiver records were processed, of which 369 produced good splitting results. We define good measurements as having a quality index greater than 0.6, a signal-to-noise ratio greater than 3, a time lag less than 4.5 ms with an error less than 0.5 ms and an error in fast polarization of less than 15°.

Fig. 5 shows cylindrical projections of the resulting splitting measurements for the stage 1 and stages 2–5 combined. Due to the array geometry, data are only available for a limited range of arrival azimuths and inclinations. Interestingly, although the full data set shows a considerable amount of scatter in fast polarization orientations, this is not apparent when viewing each stage individually. The measurements from stage 1 have predominately vertically polarized fast waves, while those from later stages show a distinctly different pattern of anisotropy with mostly horizontal polarizations.

It is not evident from Fig. 5 alone that the change splitting parameters is a temporal rather than a spatial effect, since the source locations of the two subsets do not fully coincide. The stage 1 event locations have a greater lateral extent than in the later stages resulting in greater azimuthal coverage of data. In addition, because each successive stage of the hydraulic stimulation was done at a shallower interval in the injection well, the two clusters do not cover the same depth range, although they do overlap (Fig. 2d). Since there
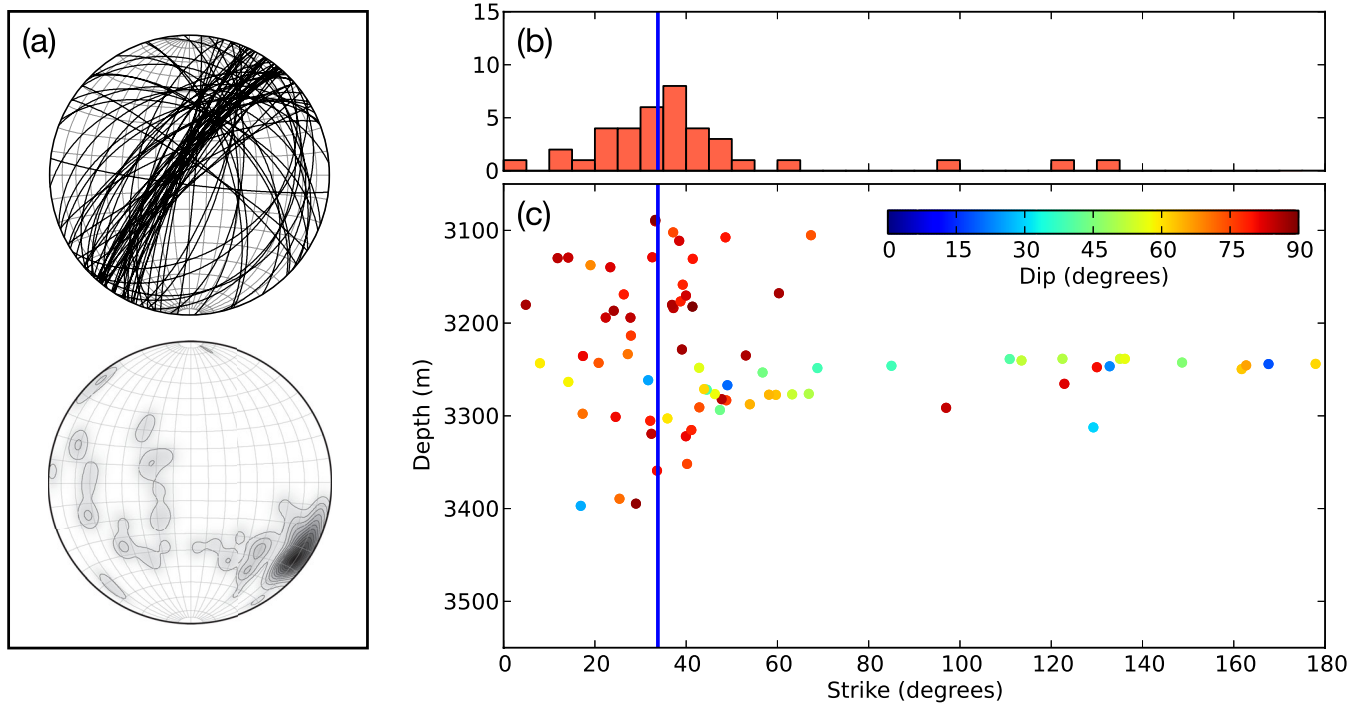
Figure 4. Open fracture orientations interpreted from image data from the treatment well, prior to fracture stimulation. (a) Stereographic projections showing fracture planes (top) and a contour map of fracture poles (bottom). (b) Histogram of the strike of steeply dipping fractures ($>70°$). (c) Scatter plot showing variation in fracture strike with depth (coloured by dip). This shows that steeply dipping open fractures consistently strike $\sim 35 \pm 15°$.

appears to be a change in the *in situ* stresses at a depth of ~ 3300 m as evidenced by the breakout data in Fig. 3, we may also expect a variation in anisotropy with depth. Fig. 6 shows another version of Fig. 5 but with the data restricted to regions with overlapping source locations (ray azimuths of 125–170°) and within the deeper stress zone (depth <3300 m). The ray paths for these events sample the same rock volume and change in polarization between stages is still apparent. This indicates that although we cannot rule out a spatial variation in anisotropy, there is a clear temporal change.

4 FRACTURE INVERSION

To link the observed changes in splitting parameters to the development of an induced fracture network we use the rock physics-based approach of Verdon *et al.* (2009) and Verdon & Wüstefeld (2013) to invert for fracture parameters. This technique assumes an orthorhombic anisotropic system that is produced by a vertical fracture set characterized by normal and tangential compliances, Z_N and Z_T, and strike, α; that is imbedded in a background rock with VTI symmetry described by Thomsen's (1986) γ, δ and ε parameters. Fig. 1 shows an illustrative example of anisotropy predicted by horizontal layering, vertical fractures and a combination of both.

A search of the parameter space is used to create a suite of anisotropic elasticity models that are used to produce synthetic shear wave splitting measurements. These are then compared with the data, with the objective of minimizing the misfit between the modelled and measured results. For each model we compute the misfit for ψ and δV_S separately. We then normalize both misfits by their minimum values, before summing them to give the overall misfit.

The inversion scheme uses the neighbourhood algorithm (NA) method of Sambridge (1999) to search over the parameter space (Thomsen's γ, δ and ε parameters; and fracture parameters Z_T,

Z_N/Z_T and α). Unlike a global grid search, the NA method discretizes the parameter space into approximately evenly distributed geometric cells, and iteratively resamples the cells that look more promising to provide finer search coverage near minima of the misfit function. Since the NA method begins with a random sampling of the parameter space to generate the initial set of neighbourhood cells, it is possible, particularly with underconstrained problems, to converge upon different solutions in successive inversions. By inverting multiple times we can examine a suite of models that fit the data well, and provide some indication of how well constrained each of the parameters are.

The inversion requires setting background isotropic velocities and density which we estimate based on velocity model. We use $V_P = 4850$ m s^{-1}, $V_S = 3200$ m s^{-1} and $\rho = 2400$ kg m^{-3}. Synthetic model analysis by both Wuestefeld *et al.* (2011) and Verdon & Wüstefeld (2013) have shown that inverted fracture parameters are relatively insensitive to errors in background velocities.

Since the splitting data show a significant change between stage 1 and 2, but with no substantial difference between the later stages, we arrange the data into two groups for the inversion: stage 1 and stages 2–5. Figs 7 and 8 show the range of inverted parameters for each group after 100 inversions. The Thomsen parameters δ and ε are not shown as they cannot be fully resolved with S-wave data alone as they trade-off against each other, although they are still included as free parameters in the inversions (Wuestefeld *et al.* 2011; Verdon & Wüstefeld 2013). We find, however, that γ is well resolved in both cases.

For the fracture properties, the stages 2–5 group shows the widest variance of inverted parameters (Fig. 8). Most of the inverted fracture strikes ranged between approximately 55° and 85°, with the lower bound agreeing reasonably well with the NE–SW orientation of the induced fracture network (Fig. 2a). Z_N/Z_T shows a broad range of inverted values, but with a clear central peak around 0.65.
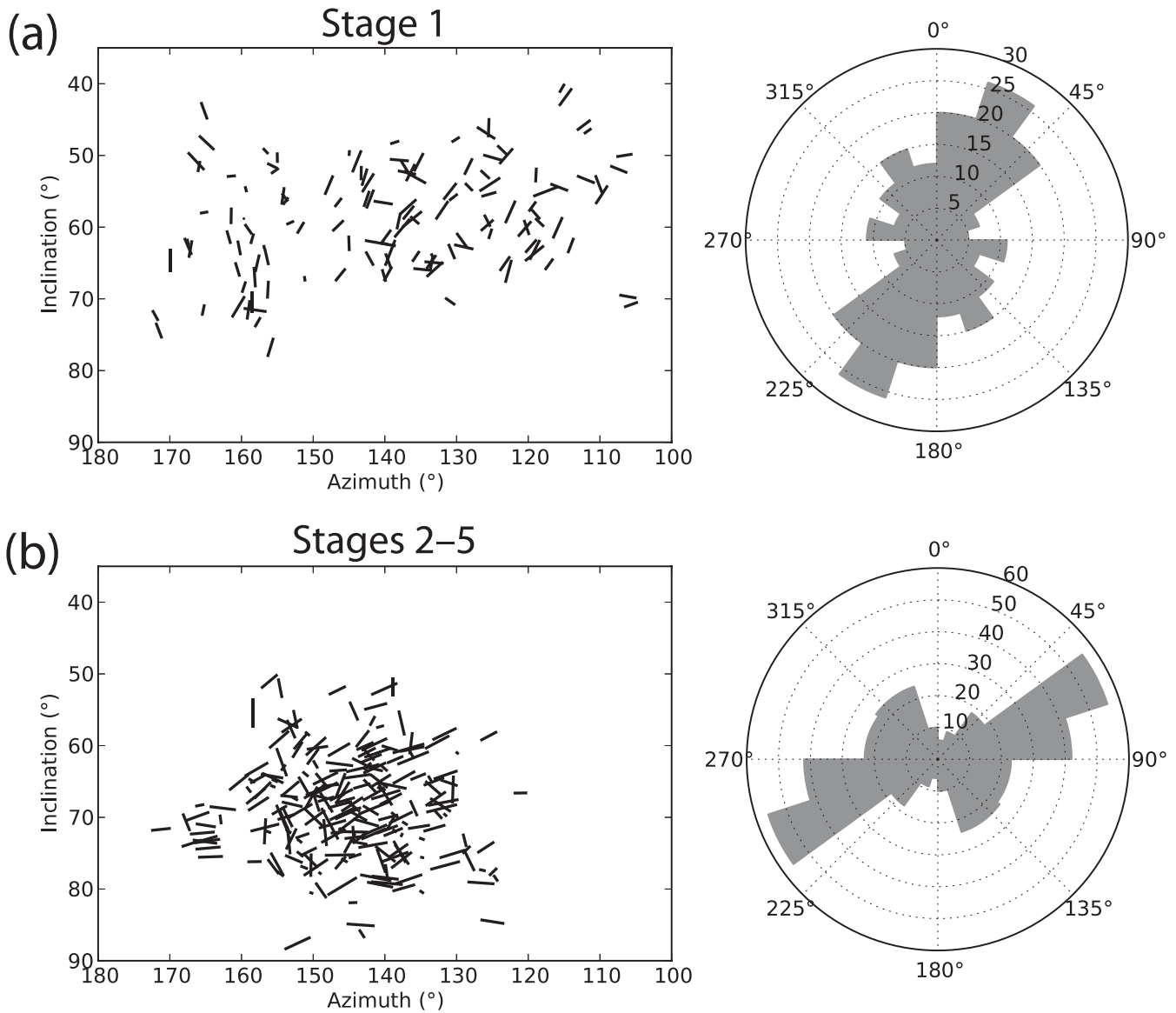
Figure 5. Left: Cylindrical projections of shear wave splitting measurements for stage 1 (a) and stages 2–5 (b). The *x*- and *y*-axes give the arrival angles of the *S* waves used to measure splitting. Tick orientations indicate the fast splitting polarization, with a vertical tick indicating a quasi-vertical *S* wave (qS_V), and a horizontal tick indicating an S_H wave. The length of the tick marks are proportional to the percentage difference between the fast and slow *S*-wave velocities (δV_S). Right: Rose diagrams showing the fast polarization orientations, Note that, there is a distinct rotation in the dominant fast polarizations after the initial stage.

There also appears to be a slight trade-off between Z_N/Z_T and strike, with high values of Z_N/Z_T favouring NE–SW strikes and low values favouring E–W strikes. Conversely, Z_T is very poorly resolved. This is likely caused by the lack of ray coverage due to unfavourable source–receiver geometry. Verdon *et al.* (2009) showed through synthetic tests that Z_T (or fracture density in their test), is difficult to constrain when most ray paths are close to the fracture normal direction, which they would be in the case of NE striking fractures. The inversion yielded a mild background VTI anisotropy characterized by $\gamma \sim 0.02$, producing approximately 2 per cent anisotropy for horizontally propagating waves.

The stage 1 inversions show much less variability, but are considerably more difficult to interpret (Fig. 7). The vast majority of the inversions converged on a fracture model with $Z_T = 1.5 \times 10^{-12}$ Pa^{-1}, $Z_N/Z_T \sim 1$ and a strike of 130°. However, the existence of a NW–SE striking natural fracture set is not supported by the borehole

data (Fig. 4), nor would we expect these fractures to remain open in a NE-oriented compressive stress field. Examination of the stage 1 inverted fracture models in Fig. 7 shows that although most models converge on this seemingly incompatible fracture model (labelled A), there is a second group of models that cluster around distinctly different parameters (labelled B). These models have a higher Z_N ($\sim$6–9 × 10^{-12} Pa^{-1}), a lower Z_N/Z_T ($\sim$0.3) and a strike of 30°, which is remarkably consistent with the borehole data. In all cases γ was found to be approximately zero, suggesting that the background rock is nearly isotropic and most of the splitting may be attributed to fractures.

Fig. 9 shows examples of predicted shear wave splitting compared to data, for the two inverted fracture models in stage 1 (A and B) and one example from stage 2–5. the models used are indicated as coloured dots on the scatter plots of Figs 7 and 8. Although models A and B produce very different patterns of anisotropy over the full
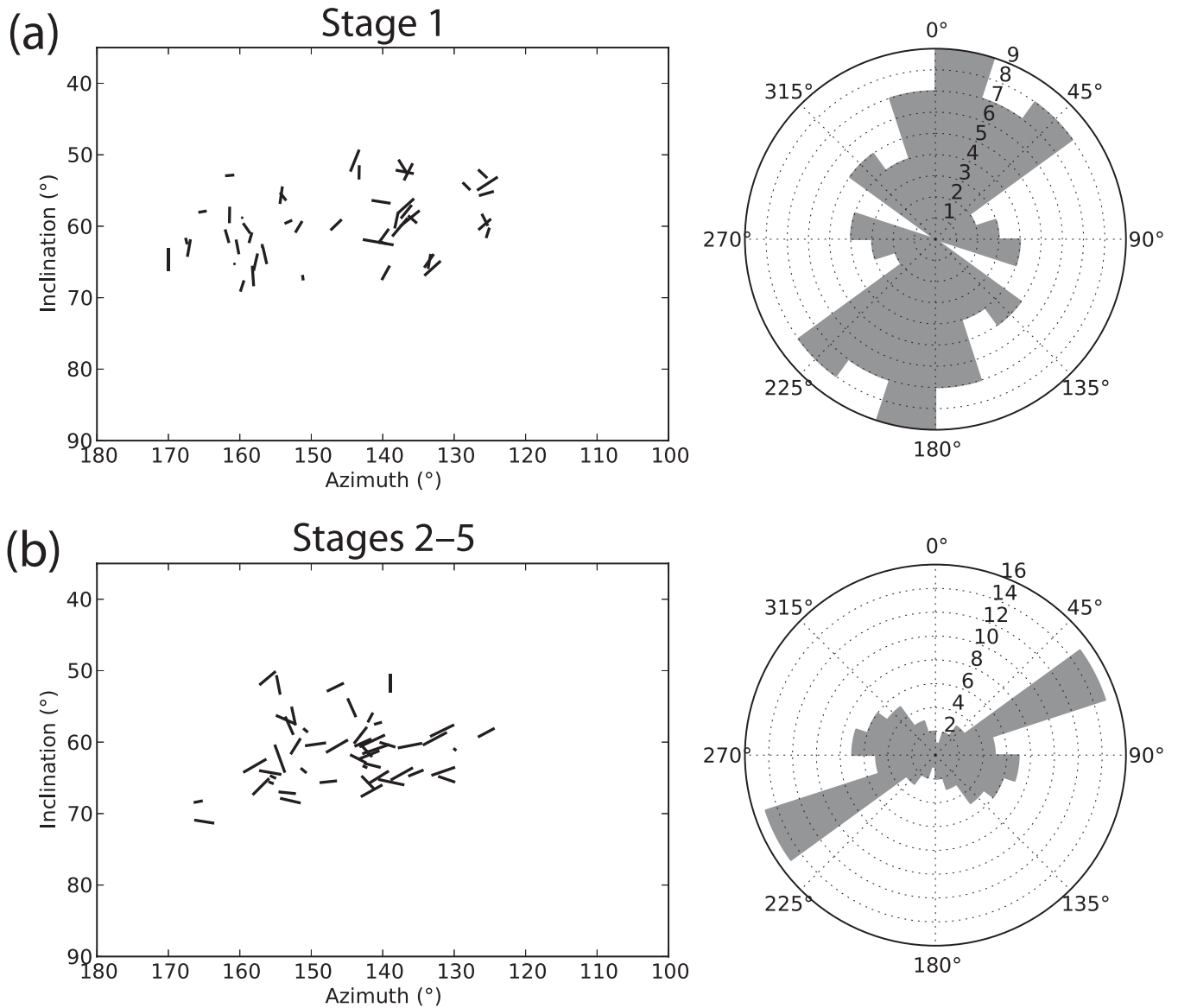
Figure 6. Shear wave splitting measurements and polarizations as in Fig. 5 but showing only data from overlapping regions of the stage 1 and stages 2–5 groups. Data are restricted to azimuths of 125–170°, and source depths <3300 m. The distinct rotation in fast polarization direction is still apparent in this restricted data set indicating that it is a temporal effect.

hemisphere, within the limited range of azimuth and inclination where data are available they are quite similar, and both match the data very well.

5 DISCUSSION

A great difficulty in interpreting the shear wave splitting results is the large change in polarizations observed. In many crustal studies, fast polarization direction is used as a proxy for the stress orientation due to stress-aligned microcracks, which may be perturbed by structural features (e.g. Boness & Zoback 2006; Gao et al. 2011; Hurd & Bohnhoff 2012). Such interpretations have been used to infer local stress reorientations due to magmatic processes in active volcanoes from temporal variations in polarization (e.g. Gerst & Savage 2004; Savage *et al.* 2010; Johnson & Savage 2012). However, these studies all used surface seismometers to measure shear wave splitting from subvertical ray paths. For lower angle arrivals this interpretation may not hold due to increased contribution of

intrinsic anisotropy (assuming VTI symmetry). In addition, even without intrinsic anisotropy, the fast polarization direction may not align with the fracture strike for waves arriving along ray paths that are strongly oblique to the fracture plane. In this case the main controlling parameter is Z_N/Z_T.

Fig. 10 shows the predicted shear wave splitting for two fracture models, which are identical except for differing Z_N/Z_T (0.1 versus 0.9). For waves propagating parallel to the fracture, splitting is controlled entirely by Z_T and both models produce the same results. For high Z_N/Z_T (~1), δV_S decreases as the propagation direction diverges from fracture-parallel to until eventually reaching zero normal to the fracture; however, ψ remains fracture-parallel for all ray paths. Conversely, if Z_N/Z_T is sufficiently low ($< \sim 0.5$) then δV_S decays to zero before reaching the normal direction, at which point the previous slow wave begins to overtake the fast wave resulting in a 90° flip in ψ.

Exactly what value of Z_N/Z_T is appropriate is unclear. Published estimates of Z_N/Z_T from laboratory and field studies show a wide
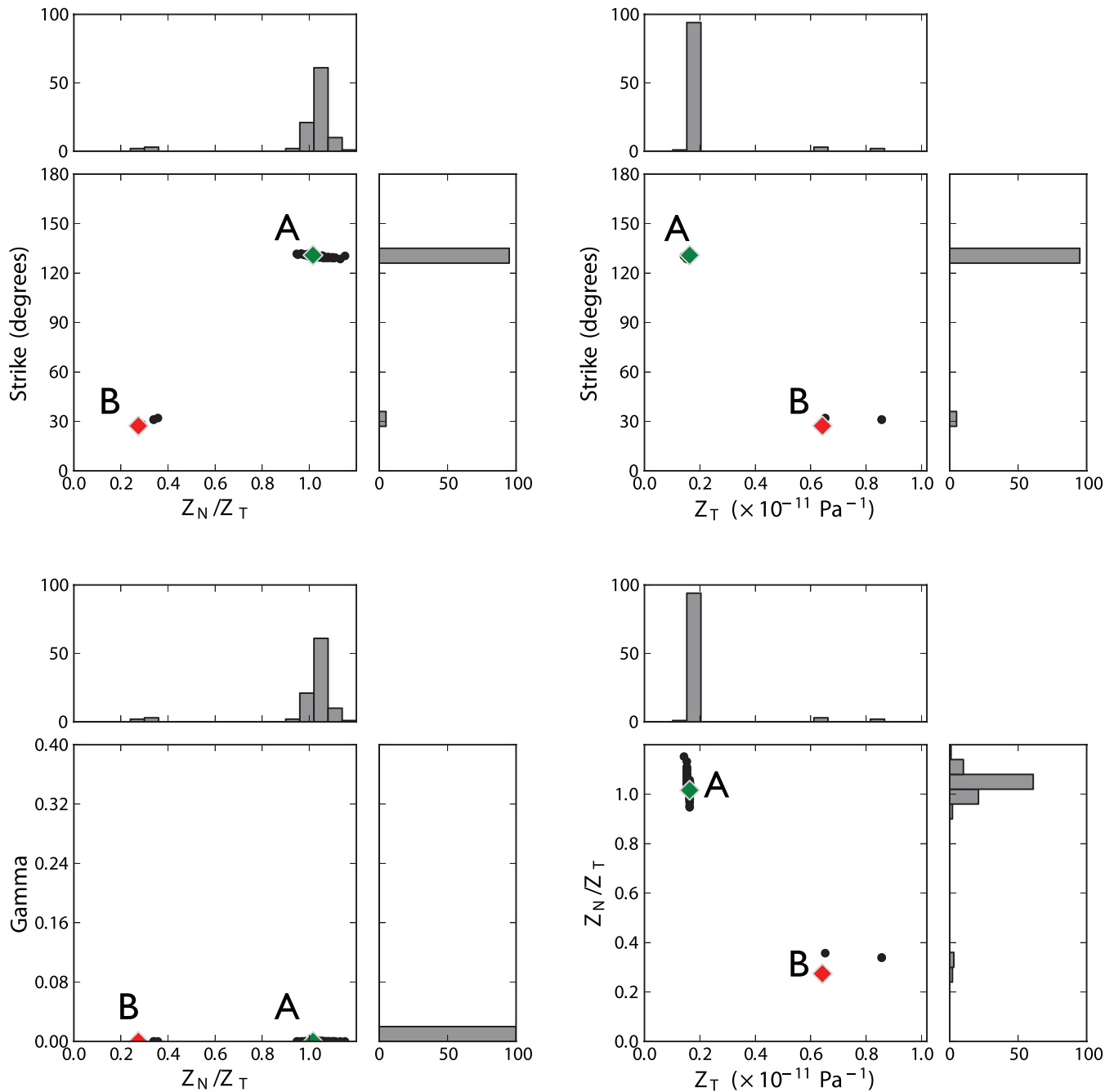
Figure 7. Results of 100 inversions of the stage 1 data set to solve for the fracture parameters Z_T, Z_N/Z_T and strike; and Thomsen's γ parameter. Labels A and B indicate two distinct clusters of fracture models that fit the data. The red and green diamonds indicate the models shown in Fig. 9.

range of values (see Verdon & Wüstefeld 2013, for a review). Many effective medium theories for modelling fractured rock assume that fractures can be described as rotationally invariant 'penny-shaped' cracks (e.g. Hudson 1981; Sayers & Kachanov 1995; Thomsen 1995). In such a model, the theoretical Z_N/Z_T for a drained crack, or equivalently one where the bulk modulus of the saturating fluid is zero, is (Sayers & Kachanov 1995):

$$Z_N/Z_T = (1 - \nu/2), \tag{1}$$

where ν is the Poisson's ratio of the intact rock. Given that ν is typically of the order 0.2 for reservoir rocks, $Z_N/Z_T \approx 1$. The special case of $Z_N/Z_T = 1$ is referred to as a 'scalar' fracture set (Schoenberg & Sayers 1995). If a fracture is fluid saturated and hydraulically iso-

lated, the relative incompressibility of an infilling fluid will act to reduce Z_N while leaving Z_T unchanged, such that $Z_N/Z_T \to 0$. However, if fluids are able to flow out of fractures in response to a passing wave, either into the rock pore–space or other adjacent fractures, then the fracture may approach the 'drained' case (i.e. $Z_N/Z_T \to 1$). The fracture's ability to drain is controlled by fracture connectivity, bulk rock permeability and fluid viscosity, as well as the frequency of the passing wave (e.g. Pointer *et al.* 2000; Chapman 2003). Most conventional reservoirs have high permeabilities, thus a scalar crack assumption may be justified, however, in an unconventional 'tight' reservoir this assumption may not be appropriate.

Another factor that may affect compliance is the internal architec-ture of natural and induced fractures, which can differ substantially
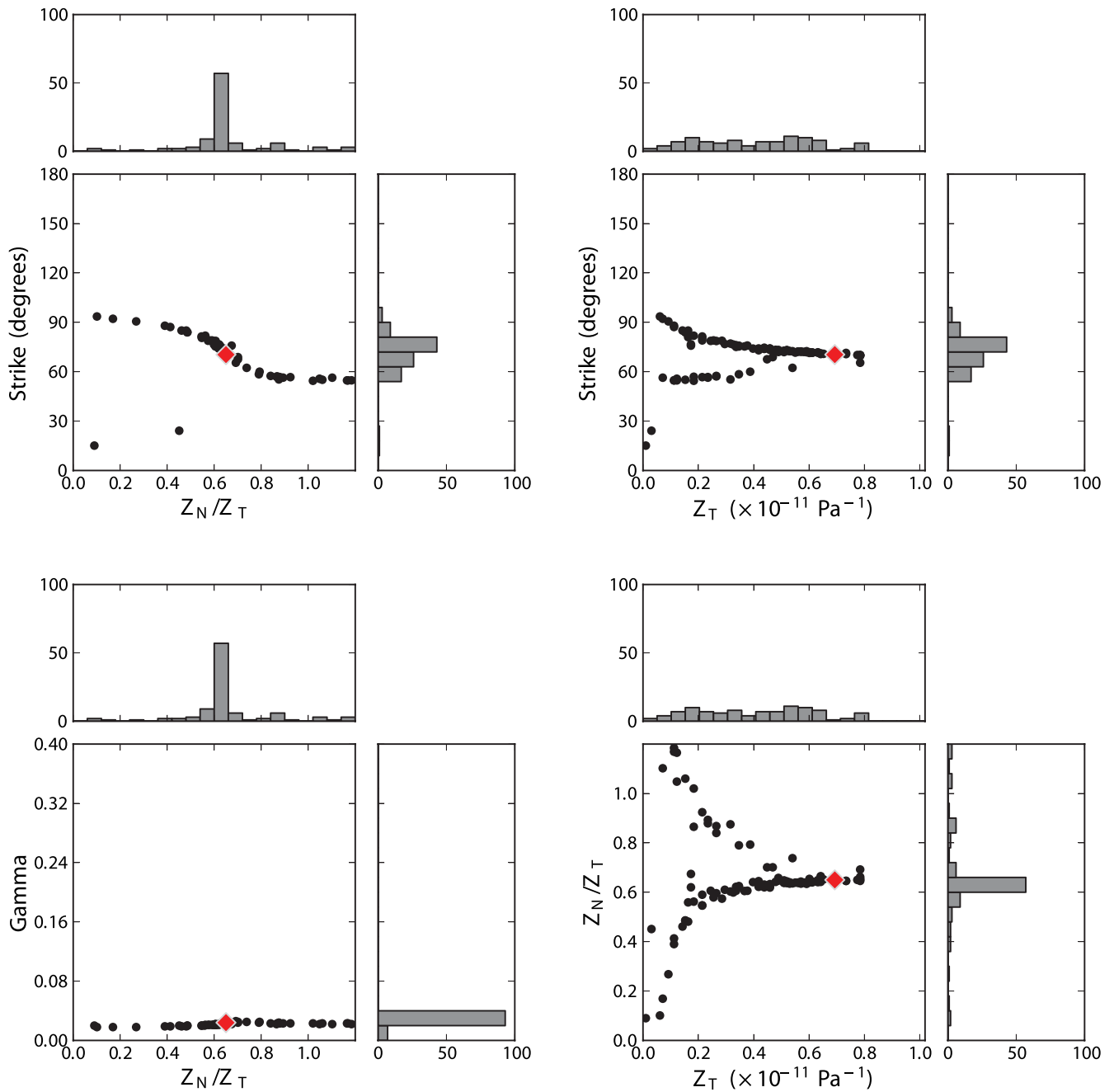
Figure 8. Results of 100 inversions of the stages 2–5 data set to solve for the fracture parameters Z_T, Z_N/Z_T and strike; and Thomsen's γ parameter. The red diamond indicates the model shown in Fig. 9.

from the idealized 'penny-shaped' crack model. Fractures can be better described as complex irregular surfaces in partial contact, and it is the size and spatial distribution of the contact surfaces and void spaces that ultimately controls Z_N/Z_T. There is evidence to suggest mineral growth which may bridge fracture faces in old fractures, may act to lower Z_N/Z_T (Sayers *et al.* 2009), whereas newly generated smooth fractures often have high Z_N/Z_T (MacBeth & Schuett 2007). More recently, it has been suggested that the injection of proppant during a hydraulic fracture stimulation may increase the effective Z_N/Z_T (Verdon & Wüstefeld 2013).

In addition to the apparent change in vertical fracture parameters, the inversions also indicate a small change in the VTI anisotropy, from $\gamma = 0$ (approximately isotropic) to $\gamma = 0.02$. This may be explained in part by a variation in intrinsic anisotropy with depth.

The effect of VTI anisotropy should be dominant for subhorizontal ray paths, which we only sample with the shallower events in the later stages. Alternatively, the increase in γ may be the result of the opening of horizontally aligned fractures in addition to vertical fractures. Fig. 4 shows that there is a damage zone between depth of 3200–3300 m with shallower fracture dips. Reactivation and extension of these fractures could result in increased VTI anisotropy.

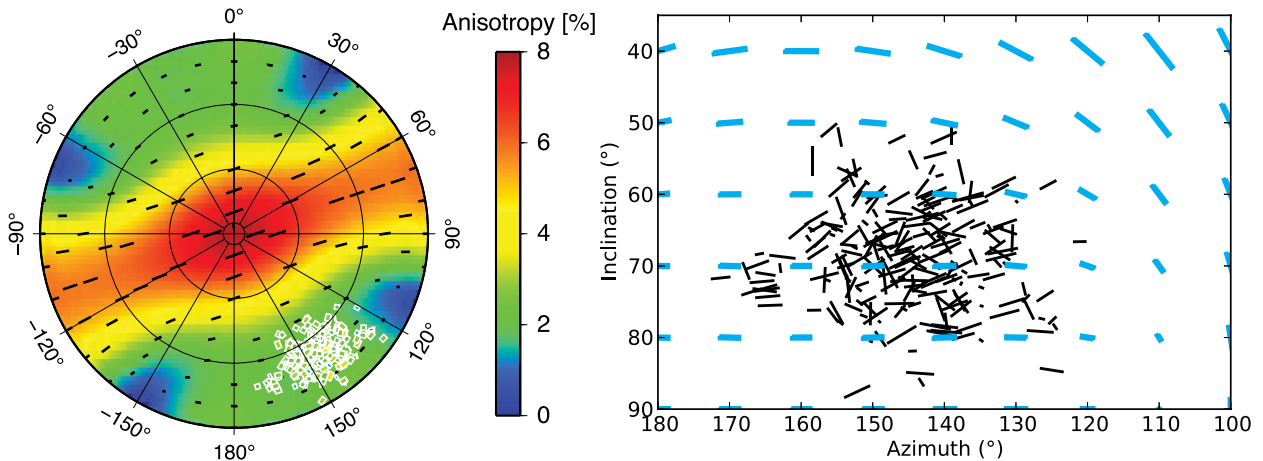## 6 CONCEPTUAL MODEL OF HYDRAULIC FRACTURING

Fig. 11 shows a proposed scenario explaining the variation in shear wave splitting observed during the fracture stimulation. Prior to
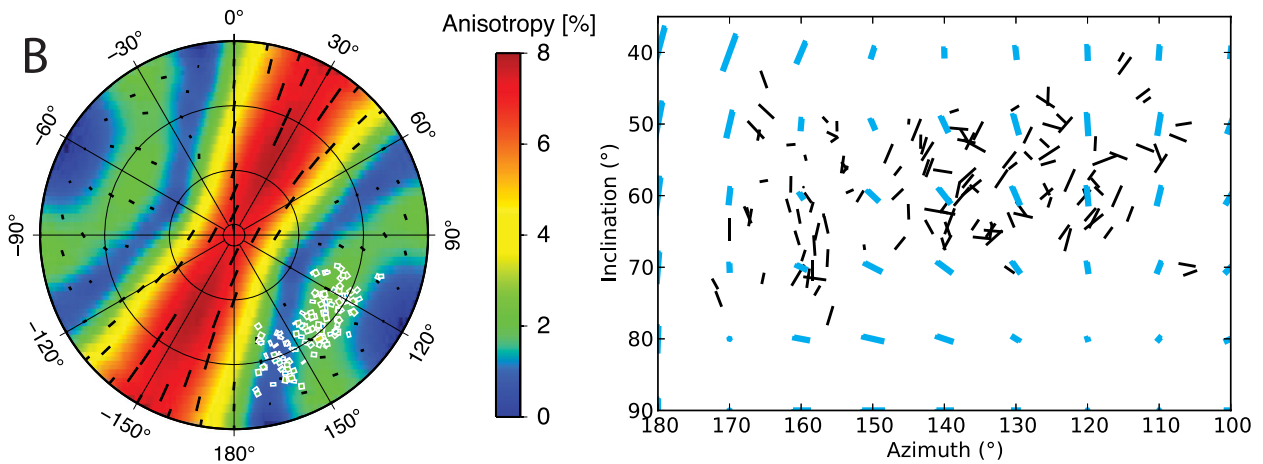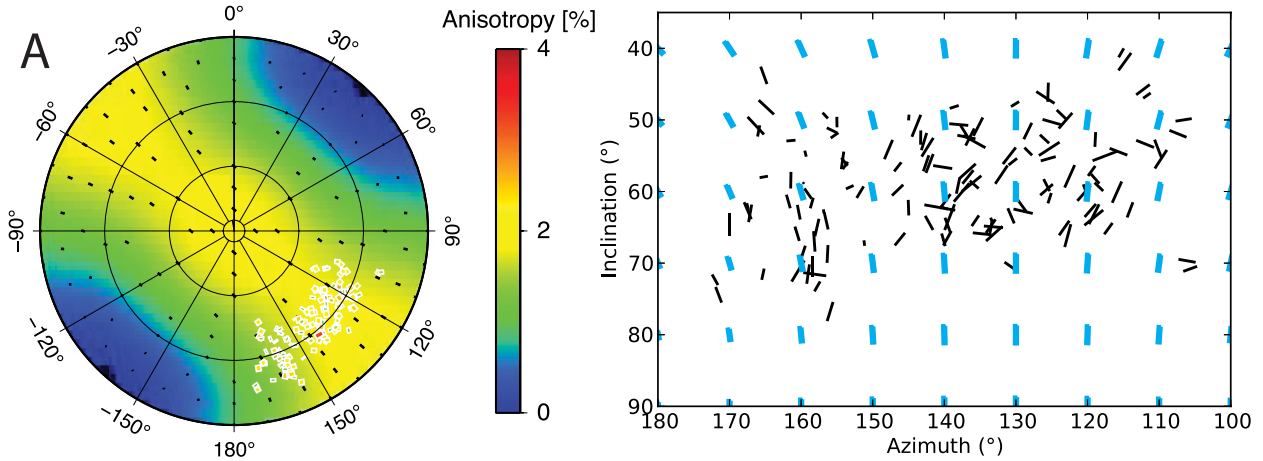
Figure 9. SWS data and inverted models for two cases of the stage 1 data (top A and B), and one case from the stages 2–5 data (bottom). Models chosen are indicated in Figs 7 and 8. Left panels show an upper hemisphere projection of the data (white outlined ticks), and the modelled SWS magnitude, δV_S (contours and tick lengths), and fast wave polarization, ψ (black tick orientations). Right panels show cylindrical projections, as in Fig. 5 of the measured SWS data (black), compared to the modelled data (blue).
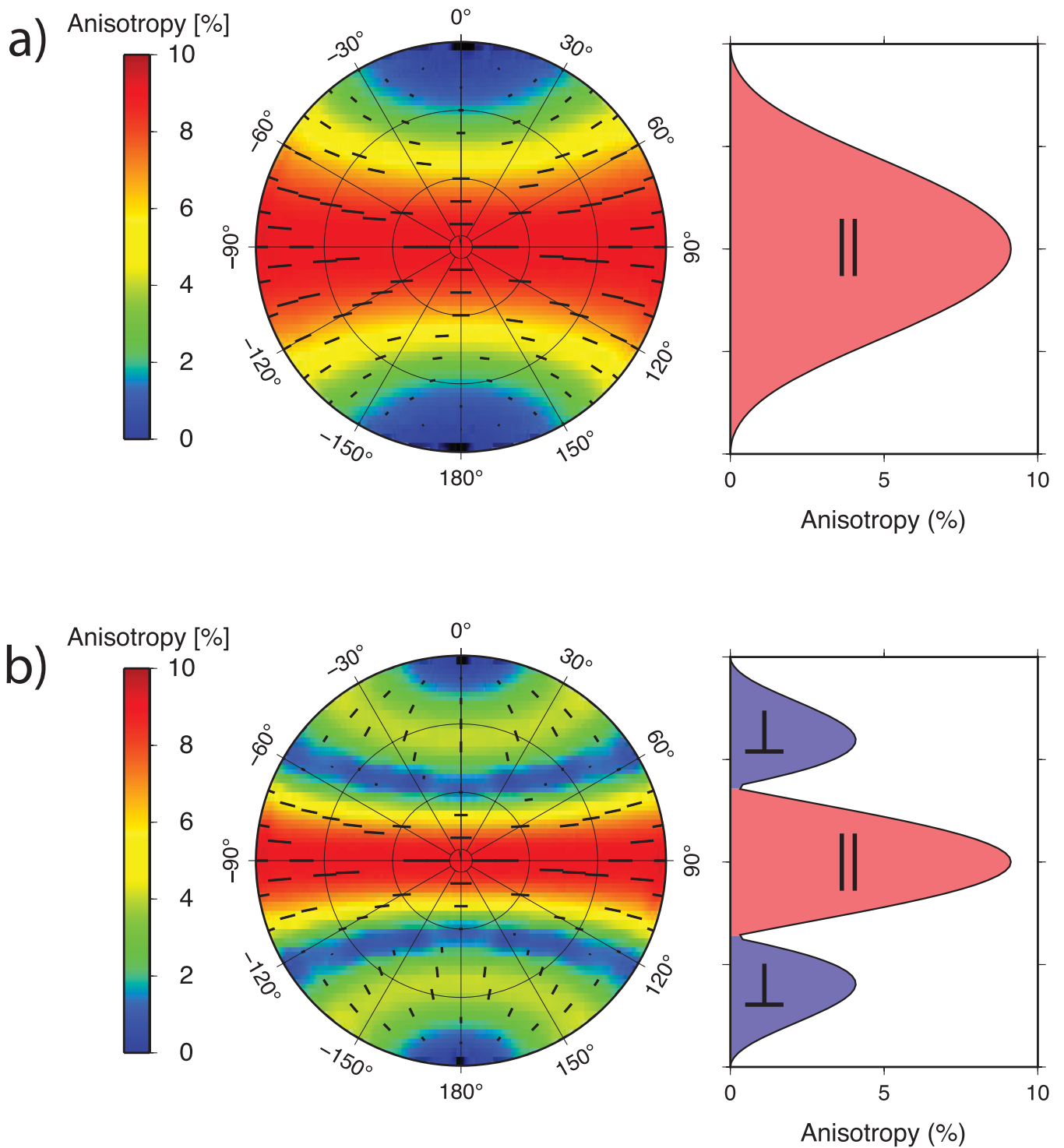
Figure 10. Predicted pattern of shear wave splitting for vertical fracture models with: (a) $Z_N/Z_T = 0.9$ (equivalent to a drained penny-shaped crack model), and (b) $Z_N/Z_T = 0.1$ (an isolated crack with a stiff saturating fluid). Plot on right indicates variation in shear wave splitting magnitude (δV_S) for different propagation azimuths relative to the fracture normal direction. Shading indicates whether fast polarization (ψ) is oriented parallel (red), or perpendicular (blue) to the fracture strike. While shear wave splitting fast polarization directions are often interpreted as aligning parallel to the fracture, this is not the case for ray paths oblique to a fracture set with low Z_N/Z_T.

stimulation there is an initial dominant fracture orientation of ~30° based on borehole data (Fig. 4). Since these are old fractures, they are likely partially cemented, and can be considered 'undrained' due to the low permeability of the reservoir. Both of these characteristics would act to lower the effective Z_N/Z_T. During stage 1 of the

hydraulic stimulations, new fractures begin to propagate parallel to S_H, which is oriented ~45–50°, slightly oblique to the natural fracture orientation. Microseismic events occur at the tips of these newly generated fractures producing shear waves that propagate out into the surrounding unstimulated rock volume, thus sampling the
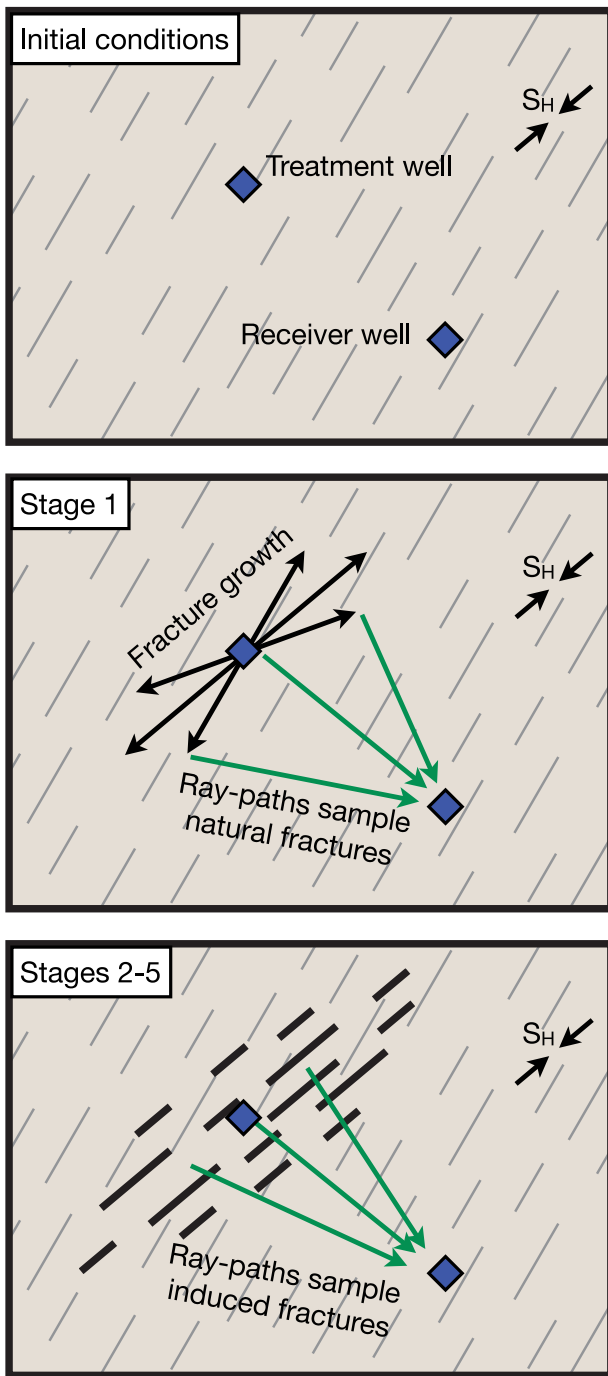
Figure 11. Conceptual model of fracturing process. Initial conditions: Natural fractures strike $\sim30°$, slightly oblique to S_H (~45–$50°$). Fractures are likely 'undrained' due to the low permeability of the reservoir, and partially cemented producing a low Z_N/Z_T of 0.3. Stage 1: Induced fractures propagate parallel to S_H, microseismic events lead the fracture propagation with ray paths largely sampling the surrounding country rock and natural fractures. Stages 2–5: Events are located largely within pre-fractured and propped rock, thus ray paths sample these new, clean fractures, which have enhanced permeability and fluid connectivity, such that they can be considered 'drained' and therefore have a higher Z_N/Z_T or 0.6.

natural fractures. Due to the low Z_N/Z_T of the fractures and the oblique propagation direction, the fast polarization does not align with the fracture strike. The newly stimulated fracture network is formed through the reactivation of natural fractures, breaking their

cemented bridges and through the generation of new fractures connecting the natural fractures together and enhancing permeability. The injection of proppant into the stimulated volume forces fractures to remain open, further enhancing permeability. The net effect is that the fractures in the stimulated volume are cleaner (i.e. smoother, and less cemented), and have greater fluid connectivity, than the pre-existing natural fractures. Later stages produce microseismicity contained largely within the stimulated volume, such that the shear waves sample the new higher Z_N/Z_T fractures. Given that S_H in the shallower portion of the stimulated volume appears to be rotated clockwise relative to the and has lower stress anisotropy (Fig. 3), it is likely that the later stages produce a more complex fracture network-oriented ENE, which is consistent with the later stage inversions.

7 CONCLUSIONS

We have conducted shear wave splitting analyses of microseismic events from a multistage hydraulic fracture stimulation. The data, which cover a relatively narrow azimuth and inclination range, show a substantial rotation in fast polarization between events from stage 1 and those from later stages. The data were inverted for intrinsic anisotropy and fracture properties, revealing two potential models to explain the observed rotation:

(1) A large (50–70°) rotation in the dominant fracture strike from SE (130°) in stage 1 to ENE (~55–$85°$) in the later stages.
(2) Both fracture sets striking in the NE quadrant, but with a smaller (20–30°) clockwise rotation coupled with an increase in Z_N/Z_T from 0.3 to 0.6.

The first model is the dominant result from the shear wave splitting inversion alone; however, the initial fracture strike is difficult to explain given the orientation of S_H, and is inconsistent with borehole fracture data. Conversely, the model 2-inferred strike is consistent with borehole data and is our preferred model. Similarly, the clockwise sense of the inferred fractures is in agreement with the misalignment between the natural fracture strike and S_H.

Large rotations (or flips) in fast polarization do not necessarily imply large changes in crack orientation. Instead it may be the result of an increase in Z_N/Z_T related to the generation of new fractures and enhanced fracture connectivity and permeability. It is important to recognize, however, that our ability to image Z_N/Z_T is limited in part by the available ray coverage. The large azimuthal variation in fast polarization for a low Z_N/Z_T model, coupled with a narrow azimuthal range of data resulted in the inversion of two compatible models, which we would not be able to discriminate between without additional information. This could be resolved with the addition of a second downhole array to extend the azimuthal coverage, greatly increasing the effectiveness of the inversions.

These observations have direct and important implications for understanding fluid flow behaviour of fractured reservoirs. The ability to remotely detect changes in Z_N/Z_T through microseismic monitoring, and therefore infer changes in fracture flow properties, provides a powerful tool for fracture characterization in a range of geological settings where hydraulic stimulation facilitates fluid flow.

REFERENCES

Alkhalifah, T., 1997. Velocity analysis using nonhyperbolic moveout in transversely isotropic media, *Geophysics,* **62**(6), 1839–1854.

van der Baan, M. & Kendall, J.-M., 2002. Estimating anisotropy parameters and traveltimes in the τ-p domain, *Geophysics,* **67**(4), 1076–1086.

Backus, G.E., 1962. Long-wave elastic anisotropy produced by horizontal layering, *J. geophys. Res.,* **67**(11), 4427–4440.

Boness, N. & Zoback, M., 2006. Mapping stress and structurally controlled crustal shear velocity anisotropy in California, *Geology,* **34**(10), 825–828.

Chambers, K., Kendall, J.-M., Brandsberg-Dahl, S. & Rueda, J., 2010. Testing the ability of surface arrays to monitor microseismic activity, *Geophys. Prospect.,* **58**(5), 821–830.

Chapman, M., 2003. Frequency-dependent anisotropy due to meso-scale fractures in the presence of equant porosity, *Geophys. Prospect.,* **51**(5), 369–379.

Crampin, S., 1984. Effective anisotropic elastic constants for wave propagation through cracked solids, *Geophys. J. R. astr. Soc.,* **76**(1), 135–145.

Gao, Y., Wu, J., Fukao, Y., Shi, Y. & Zhu, A., 2011. Shear wave splitting in the crust in North China: stress, faults and tectonic implications, *Geophys. J. Int.,* **187**(2), 642–654.

Gerst, A. & Savage, M., 2004. Seismic anisotropy beneath Ruapehu volcano: a possible eruption forecasting tool, *Science,* **306**(5701), 1543–1547.

Hall, S.A. & Kendall, J.-M., 2003. Fracture characterization at Valhall: application of P-wave amplitude variation with offset and azimuth (AVOA) analysis to a 3D ocean-bottom data set, *Geophysics,* **68,** 1150–1160.

Hudson, J., 1980. Overall properties of a cracked solid, in *Mathematical Proceedings of the Cambridge Philosophical Society,* Vol. **88,** Cambridge University Press, pp. 371–384.

Hudson, J., 1981. Wave speeds and attenuation of elastic waves in material containing cracks, *Geophys. J. R. astr. Soc.,* **64**(1), 133–150.

Hurd, O. & Bohnhoff, M., 2012. Stress- and structure-induced shear-wave anisotropy along the 1999 Izmit rupture, northwest Turkey, *Bull. seism. Soc. Am.,* **102**(5), 2177–2188.

Johnson, J. & Savage, M., 2012. Tracking volcanic and geothermal activity in the Tongariro Volcanic Centre, New Zealand, with shear wave splitting tomography, *J. Volc. Geotherm. Res.,* **223,** 1–10.

Kendall, J.-M. *et al.*, 2007. Seismic anisotropy as an indicator of reservoir quality in siliciclastic rocks, *Geol. Soc. Lond. Spec. Publ.,* **292**(1), 123–136.

Lynn, H.B. & Thomsen, L.A., 1990. Reflection shear-wave data collected near the principal axes of azimuthal anisotropy, *Geophysics,* **55**(2), 147–156.

MacBeth, C. & Schuett, H., 2007. The stress dependent elastic properties of thermally induced microfractures in aeolian Rotliegend sandstone, *Geophys. Prospect.,* **55**(3), 323–332.

Maxwell, S., 2010. Microseismic: growth born from success, *Leading Edge,* **29**(3), 338–343.

Pointer, T., Liu, E. & Hudson, J., 2000. Seismic wave propagation in cracked porous media, *Geophys. J. Int.,* **142**(1), 199–231.

Sambridge, M., 1999. Geophysical inversion with a neighbourhood algorithm–I. searching a parameter space, *Geophys. J. Int.,* **138**(2), 479–494.

Savage, M., Ohminato, T., Aoki, Y., Tsuji, H. & Greve, S., 2010. Stress magnitude and its temporal variation at Mt. Asama Volcano, Japan, from seismic anisotropy and GPS, *Earth planet. Sci. Lett.,* **290**(3–4), 403–414.

Sayers, C. & Kachanov, M., 1995. Microcrack-induced elastic wave anisotropy of brittle rocks, *J. geophys. Res.,* **100,** 4149–4149.

Sayers, C., Taleghani, A. & Adachi, J., 2009. The effect of mineralization on the ratio of normal to tangential compliance of fractures, *Geophys. Prospect.,* **57**(3), 439–446.

Schoenberg, M. & Sayers, C.M., 1995. Seismic anisotropy of fractured rock, *Geophysics,* **60,** 204–211.

Thomsen, L., 1986. Weak elastic anisotropy, *Geophysics,* **51**(10), 1954–1966.

Thomsen, L., 1995. Elastic anisotropy due to aligned cracks in porous rock, *Geophys. Prospect.,* **43**(6), 805–829.

Tsvankin, I. & Thomsen, L., 1994. Nonhyperbolic reflection moveout in anisotropic media, *Geophysics,* **59**(8), 1290–1304.

Valcke, S.L.A., Casey, M., Lloyd, G.E., Kendall, J.-M. & Fisher, Q.J., 2006. Lattice preferred orientation and seismic anisotropy in sedimentary rocks, *Geophys. J. Int.,* **166**(2), 652–666.

Verdon, J.P. & Wüstefeld, A., 2013. Measurement of the normal/tangential fracture compliance ratio (Z_N/Z_T) during hydraulic fracture stimulation using S-wave splitting data, *Geophys. Prospect.,* **61**(Suppl. 1), 461–475.

Verdon, J.P., Kendall, J.-M. & Wüstefeld, A., 2009. Imaging fractures and sedimentary fabrics using shear wave splitting measurements made on passive seismic data, *Geophys. J. Int.,* **179**(2), 1245–1254.

Vernik, L. & Nur, A., 1992. Ultrasonic velocity and anisotropy of hydrocarbon source rocks, *Geophysics,* **57**(5), 727–735.

Wuestefeld, A., Al-Harrasi, O., Verdon, J.P., Wookey, J. & Kendall, J.-M., 2010. A strategy for automated analysis of passive microseismic data to image seismic anisotropy and fracture characteristics, *Geophys. Prospect.,* **58**(5), 755–773.

Wuestefeld, A., Verdon, J.P., Kendall, J.-M., Rutledge, J., Clarke, H. & Wookey, J., 2011. Inferring rock fracture evolution during reservoir stimulation from seismic anisotropy, *Geophysics,* **76**(6), WC159–WC168.